Research Article | Vol. 27, No. 14 | 8 Jul 2019 | OPTICS EXPRESS 19448
Optics EXPRESS

Ruling engine using adjustable diamond and interferometric control for high-quality gratings and large echelles

XIAOTAO MI,[1,2,5] SHANWEN ZHANG,[1,2,3] XIANGDONG QI,[1,2,4] HAILI YU,[1,2] HONGZHU YU,[1,2] AND YUGUO TANG[1,2]

[1]*Changchun Institute of Optics, Fine Mechanics and Physics, Chinese Academy of Sciences, Changchun, Jilin 130033, China*
[2]*National Engineering Research Center for Diffraction Gratings Manufacturing and Application, Changchun, Jilin 130033, China*
[3]*zhshwen007@163.com*
[4]*chinagrating@263.net*
[5]*mixiaotao_ciomp@126.com*

Abstract: A concept for position adjustment of the diamond in a ruling engine to enable nanoscale groove positioning is proposed. Based on this concept, we fabricate a diamond carriage, design an optical path, and propose an appropriate control method. Several high-quality gratings are ruled for spectrometer or interferometer applications. After implementation of the improvements, the maximum intensity of ghosts and scattered light of the echelle grating with 79 grooves/mm is reduced to half of that before the improvement, and the highest achievable groove density is increased from 6000 grooves/mm to 8000 grooves/mm. The grating ruling results indicate that the proposed concept and the related improvements to the engine significantly improve the accuracy of the CIOMP-6 ruling engine.

1. Introduction

The excellent functions of gratings, including dispersion, polarization and phase matching, have led to strong demand for these optical elements in applications ranging from spectral analysis [1,2] to lasers [3–5], optical communications [6–8] and pulse compressors [9,10]. The mechanical ruling method, which was the first method used to fabricate gratings, remains the most important way to produce gratings with high-quality and high-precision shapes such as infrared laser gratings and large-sized echelle gratings [11,12].

Recently, there has been an increasingly urgent requirement for gratings with higher precision to achieve higher performance and quality levels in the existing grating applications [13–17]. However, the accuracy of the grating ruling engine directly affects the accuracy of the ruled grating [18,19]. The development of ruling engines and ruled gratings has been in progress for more than a century, but the pursuit of higher precision in both ruling engines and ruled gratings has not stopped [20–23]. In all the early ruling engines, and in many of the later engines, both the positioning of the grooves and the final quality of the gratings were dependent on the mechanical accuracy of the component parts and the assembly accuracy of the entire engine [24,25]. The development of interferometry and closed-loop control technologies and their application to ruling engines allowed the positions of the grating grooves to be determined based on the wavelength of the light, and the overall grating performance, in terms of problems such as ghosts, light scattering and wavefront quality, improved greatly [26,27].

The major internationally known high-precision ruling engines include the MIT-C engine and the Hitachi-4 engine. The former uses a continuous-motion system with closed-loop interference control and has ruled a variety of high-precision echelle gratings with grating dimensions of up to 350 mm × 450 mm [28]. The latter uses a new type of stop-and-go operation, where a continuous screw-driving mechanism drives the lower carriage while a

#366127 https://doi.org/10.1364/OE.27.019448
Journal © 2019 Received 25 Apr 2019; revised 30 May 2019; accepted 2 Jun 2019; published 26 Jun 2019

Optics EXPRESS

closed-loop control system with a piezoelectric device executes the walking-stop motion of the grating blank; this engine can fabricate ruled gratings with maximum dimensions of 200 mm × 300 mm and demonstrated a highest groove density of 10,000 grooves/mm [29].

The early closed-loop-controlled ruling engines and the early closed-loop control method used for the CIOMP-6 engine all realized groove positioning by adjusting the blank and its carriage. However, the capability of our blank carriage to correct groove errors and the mechanical natural frequency of the blank carriage contradict each other; the mass of the inner carriage plus the large-area grating blank may be as high as several hundred kilograms, and it is quite difficult to drive such heavy loads and achieve nanometer-scale control accuracy. Recently, we proposed a new concept that involves adjustment of the position of the diamond to achieve nanoscale groove positioning. In this work, on the basis of this concept, we fabricate a new diamond carriage with an interferometer and a piezoelectric device for the measurement and correction of the groove errors. And then, considering the new diamond carriage structure, we designed the new optical path and propose the new control strategy. After the above improvements are made, the maximum intensity of ghosts and scattered light of the 79-grooves/mm echelle grating reduced to half of that before the improvement, and the highest achievable groove density is increased from 6000 grooves/mm to 8000 grooves/mm.

The objectives of this paper are to describe the new concept in detail, the improvements made to the CIOMP-6 engine and some of the high-quality gratings that were ruled after the improvements had been implemented in the engine.

2. Outline of the CIOMP-6 ruling engine

Over the past ten years, we have been fully committed to the design, manufacture and improvement of the CIOMP-6 ruling machine. In the development of this ruling engine, we have made full use of our experience in building ruling engines and fabricating ruled gratings and have proposed new concepts that differ from those of other ruling engines, including a new diamond carriage system using aerostatic guideways and new high-precision control concepts and strategies. In the reference [19], we have made a detailed introduction to the mathematical models required for the design and manufacturing of the CIOMP-6 ruling engine and the core systems of the CIOMP-6 ruling engine, including the blank carriage system, the diamond carriage system, the measurement system and the closed-loop control system. In this paper, we only provide a summary description of the ruling engine and introduce our new concept in detail.

Figure 1 shows a schematic diagram of the ruling engine, and Fig. 2 shows a photograph of the actual ruling engine. To isolate external variations, the ruling engine is mounted on a single-piece marble platform supported by 12 air springs with a natural frequency of 1 Hz. To reduce the effects of thermal deformation of the ruling engine parts on the accuracy of the ruling engine, the temperature of the room in which the ruling engine is located must be strictly controlled, and the temperature fluctuation of the core ruling area is less than ± 0.01°C. The main heat sources, which include torque motors, lasers, computers, and drives, are isolated from the core ruling area. All computers and drives are placed outside the vibration isolation platform and the ruling room.

Optics EXPRESS

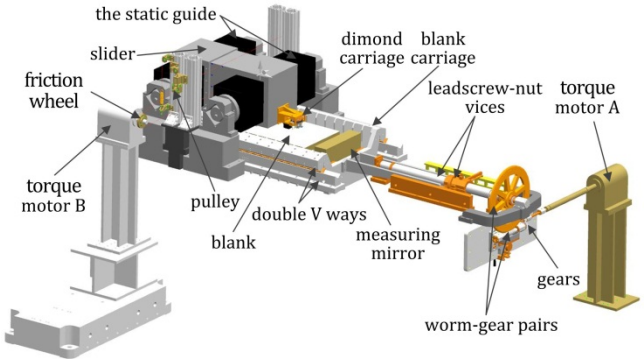

Fig. 1. Schematic diagram of the ruling engine.

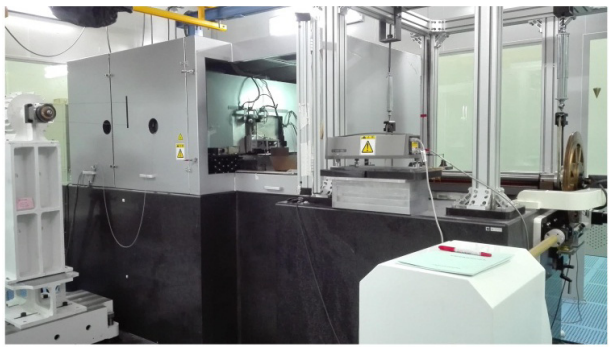

Fig. 2. Photograph of the ruling engine.

When the ruling engine is operating, the rotational motion of torque motor A is converted into a slow one-way operation of the blank carriage on the double V-ways via a set of gears, worm gear pairs and lead screw nut vices. During travel over a distance of 700 mm, the periodic errors and the cumulative errors of the transmission mechanism are 200 nm and 5 μm, respectively, while the yaw error and the pitch error of the blank carriage are both better than 0.2 arcsec. The blank carriage includes an inner carriage and an outer carriage, where the inner carriage is suspended inside the outer carriage using four parallel leaf springs, and two piezoelectric actuators are installed between the inner stage and the outer stage to correct the above mechanical errors and achieve carriage positioning with accuracy of a few nanometers.

During the process of ruling a grating, the diamond carriage travels with a reciprocating motion along the direction orthogonal to the blank carriage system. To eliminate the problems of friction, wear and vibration that may occur during the high-speed travel of the diamond carriage system, we first used aerostatic guideways in the diamond carriage system. The forward and reverse rotation of torque motor B is converted into the reciprocating motion of the slider that carries the diamond on the static guide way using a wire rope, a friction wheel and a pulley. To increase the straightness of the slider while also reducing the deflection error of the moving slider relative to that of the static guide, we used a double aerostatic guideway structure, and the wire rope was installed at the center of the slider. After the diamond carriage system is assembled, the straightness error and the deflection error of the moving slider are found to be 0.05 arcsec and 0.01 arcsec, respectively, over a translation distance of 420 mm.

3. Improvement of the CIOMP-6 ruling engine

3.1 Proposal of new precision control concept

Almost all closed-loop-controlled ruling engines and the early CIOMP-6 working mode achieved groove positioning with accuracy of within a few nanometers by adjusting the

Optics EXPRESS

position of the grating blank carriage. A schematic diagram of the blank carriage of the CIOMP-6 ruling engine is shown in Fig. 3. Two piezoelectric actuators are mounted on the outer carriage and four extension springs are used to ensure that the double piezoelectric actuators remain in close contact with the inner carriage.

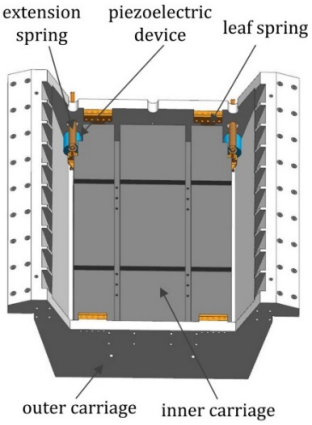

Fig. 3. Schematic diagram of blank carriage of CIOMP-6 ruling engine.

The ability of the blank carriage to correct groove errors is illustrated in Fig. 4. The red rhombus-shaped area represents the theoretical correction ability of the blank carriage, while the blue rhombus-shaped area with measurement points shows the actual measurement results for the blank carriage. However, the existing blank carriage structure faces a contradictory problem. The correction capability of the carriage will decrease as the elastic stiffnesses of the leaf spring and the extension spring increase; conversely, the mechanical natural frequency of the blank carriage will decrease, which will then affect the bandwidth of the control system. For large-area gratings, the mass of the inner carriage plus the blank may be as high as several hundred kilograms, and it is quite difficult to drive such heavy loads and achieve nanometer-scale control accuracy. However, the diamond, the tool holder and the weights on the diamond weigh less than 1 kg in total, which is beneficial when attempting to achieve high-precision control. Therefore, we propose a new method to achieve nanoscale groove positioning by controlling the position of the diamond.

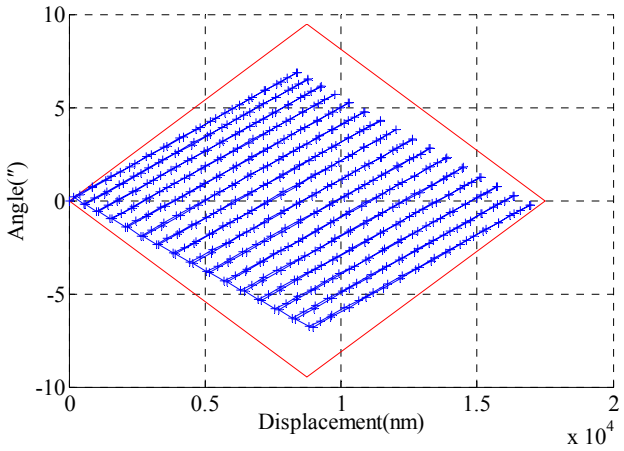

Fig. 4. Ability of the blank carriage to correct groove errors.

Optics EXPRESS

3.2 Improvement of the CIOMP-6 ruling engine

New mechanical structure

Based on the new control concept described above, we improved the mechanical structure of the CIOMP-6 ruling engine, as shown in Fig. 5. We installed an interferometer and a piezoelectric device in the diamond carriage, while the reference mirror and the diamond holder were mounted on the moving carriage of the piezoelectric device, and the measuring mirror was mounted on the blank carriage. Compared with the old diamond carriage, the new diamond carriage has the function of correcting the groove errors and the diamond carriage structure will become more complicated. As the complexity of the diamond carriage structure increases, it will bring some inconvenience to the disassembly and assembly of the diamond.

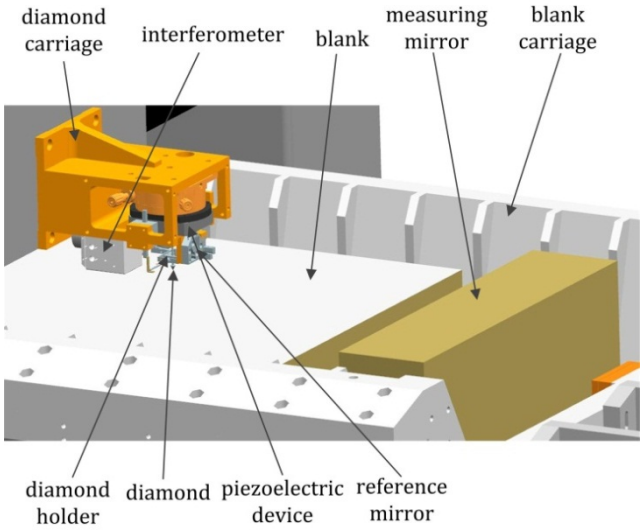

Fig. 5. Schematic diagram of the improved mechanical structure.

During the grating ruling procedure, the interferometer detects the relative positioning of the reference mirror and the measuring mirror in real time and feeds the position information back to the piezoelectric device through the control system to realize real-time adjustment of the diamond. The measuring mirror is like a high-precision standard ruler that will affect the straightness of the grating grooves directly, so we require the flatness of the measuring mirror to be as high as possible. This 100 mm × 80 mm × 420 mm measuring mirror is worked to a flatness of within $\lambda/10$ (where λ = 632.8 nm) with no abrupt departures from straightness. To reduce temperature effects, Zerdour, which is an optical glass with a low expansion coefficient, is used as the material for the measuring mirror.

New optical path structure

In the new diamond carriage, because the ruling plane and the measuring plane are separated by 31.75 mm, Abbe errors will be caused by a combination of deflection of the slider and the pitch error of the blank carriage. The deflection error and the pitch error are measured as 0.01 arcsec and 0.2 arcsec and the resulting Abbe errors are 1.6 nm and 31 nm, respectively. Therefore, it is only necessary to correct the Abbe error that is caused by the blank carriage pitch error. The new optical path is thus designed with Abbe error measurement capability while also considering the new diamond carriage structure. Compared with the old optical path structure, the new optical path structure uses two interferometers to measure the displacement error and the pitch error respectively, which is beneficial to reduce the complexity of the new diamond carriage and then improves the convenience of the diamond disassembly and assembly.

Optics EXPRESS

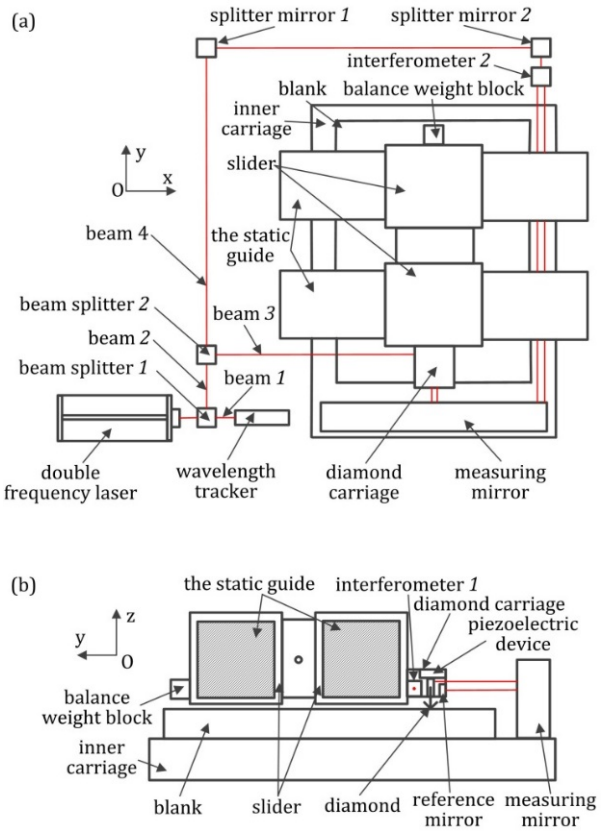

Fig. 6. New optical measurement system. (a) Top view; (b) side view.

As shown in Fig. 6, a laser beam with $\lambda = 632.8$ nm is split into two beams by beam splitter 1. Beam 1 is incident into a wavelength tracker to compensate for the errors caused by changes in the refractive index of the air. Beam 2 is further split into two beams by beam splitter 2. Beam 3 is incident into interferometer 1 to measure the displacement error between the reference mirror and the measuring mirror. Beam 4 is incident into interferometer 2 via splitter mirror 1 and splitter mirror 2, and is then used to measure the blank carriage pitch error.

New control method

In theory, the groove error can be corrected using the piezoelectric device on the diamond carriage. Compared with the old control method, to reduce the effect of the straightness error of the piezoelectric device on the groove shapes of gratings with high groove densities and on the scattered light levels of high-precision gratings operating with different working intervals and working ranges, we aim to ensure that the piezoelectric device always works within a range of ± 300 nm using the new control method.

The CIOMP-6 ruling engine uses a stop-and-go blank motion action and the piezoelectric device works on the diamond carriage during the grating ruling stage while the blank carriage system remains stationary. The working intervals and the working range of the piezoelectric device are mainly affected by yaw error and the accumulated blank carriage system error. To reduce or even eliminate these two types of error, we propose the idea of pre-positioning control before the grating ruling operation. Specifically, after the current groove has been completed, we calculate both the yaw error and the cumulative error that must be corrected from the groove data and compensate these errors separately using the piezoelectric device on the blank carriage and torque motor A of the blank carriage system before the next groove is

Optics EXPRESS

ruled. After the above compensation operation is completed, the errors required for real-time adjustment of the piezoelectric device on the diamond carriage include the straightness error of the measuring mirror, the residual yaw error and the accumulated error can be within ± 300 nm.

A schematic diagram of the proposed new control system for the CIOMP-6 ruling engine is shown in Fig. 7. This system consists of a computer with a master program and three feedback control loops with two piezoelectric devices and a torque motor that are used for groove positioning, control of the diamond system and the tool lifting control loop.

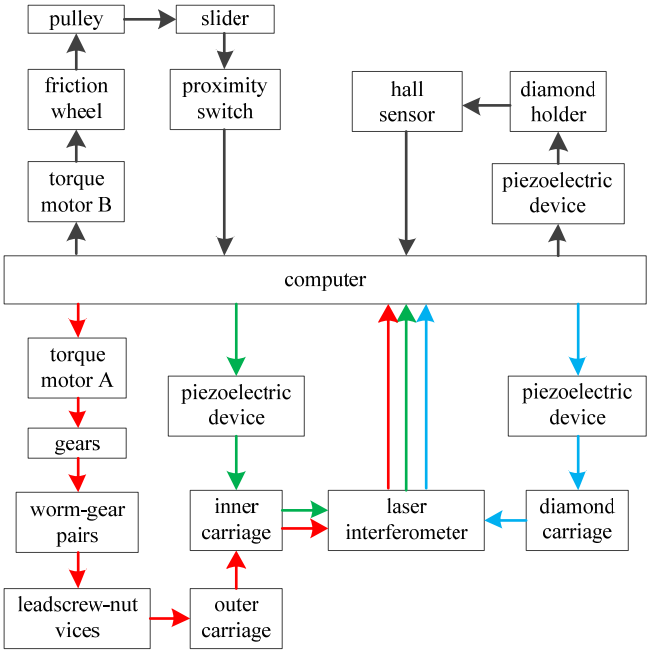

Fig. 7. Block diagram of the CIOMP-6 ruling engine control system.

4. Ruling results

After the above improvements were made, the accuracy of the CIOMP-6 ruling engine was further improved, providing the ability to rule high-groove-density gratings and large-area echelle gratings. We have already produced several high-quality gratings with high-precision shape requirements for users. In this section, we introduce the typical gratings and the capabilities of the ruling engine.

4.1 High-efficiency gratings

We have ruled three high-efficiency gratings for use in three channels of a spectrometer. This spectrometer covers the spectrum from 240 nm to 850 nm and was designed by SITP(Shanghai Institute of Technical Physics, Chinese Academy of Science) for aerospace loads.

These gratings are 25 mm × 25 mm × 6 mm gratings with groove densities of 500, 768, and 1520 grooves/mm that were blazed at 10°, 9.7°, and 12.7°, respectively. Under dark conditions, a laser beam that needs to be measured incidents on the grating surface at a designed angle of incidence, and then we use a moving power meter to measure the power including the blazed order and the ghosts or scattered light between the diffraction orders. The ratio of the maximum power of the ghosts or scattered light to the blazed order power is defined as the ghosts or scattered light intensity. No Rowland or Lyman ghosts were observed, the maximum intensity of the ghosts and the scattered light can reach 10^{-5}, and the curves for the theoretical design efficiency and the test efficiency are shown in Fig. 8. The test efficiency not only approximates the theoretical design efficiency numerically, but the curve shape is also the same, thus

Optics EXPRESS

indicating that the actual grating groove shape is basically the same as the theoretical groove shape. Figure 9 shows the wavefront values of these gratings at 632.8 nm, a blazed order of −1. As shown in Fig. 9, the peak to valley (PV) value of the 500-, 768-, and 1520-grooves/mm gratings are 0.079λ, 0.109λ and 0.145λ, respectively; the root mean square (RMS) value of the 500-, 768-, and 1520-grooves/mm gratings are 0.079λ, 0.109λ and 0.145λ, respectively.

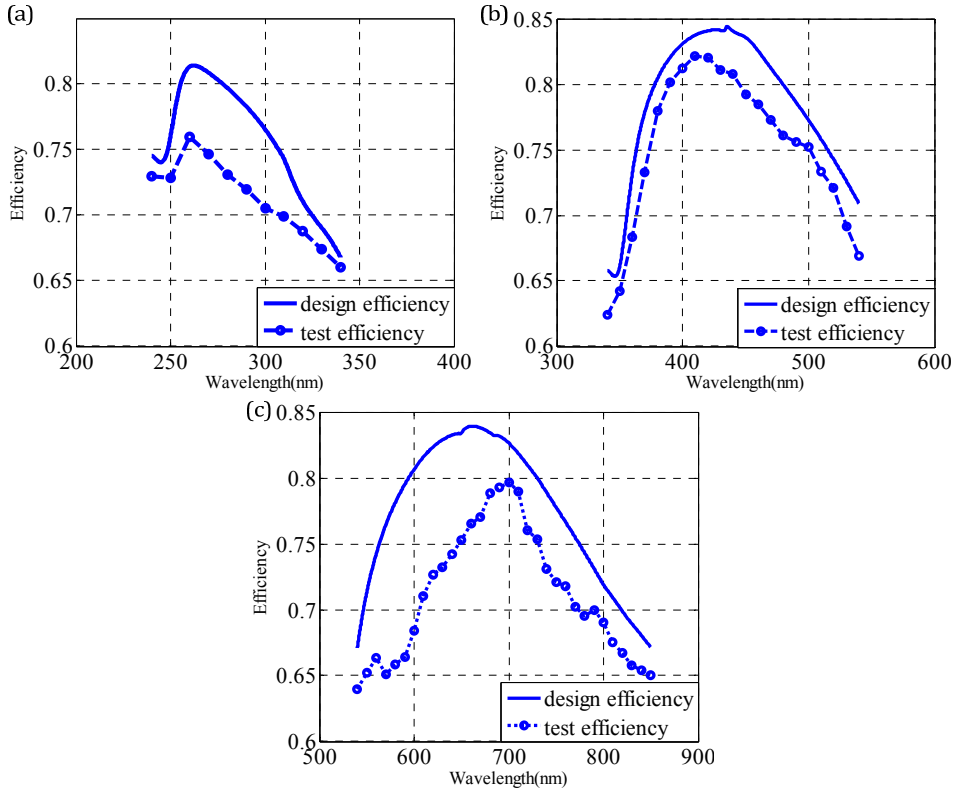

Fig. 8. Test efficiency and design efficiency of the gratings. (a) 500 grooves/mm; (b) 768 grooves/mm; and (c) 1520 grooves/mm.

Optics EXPRESS

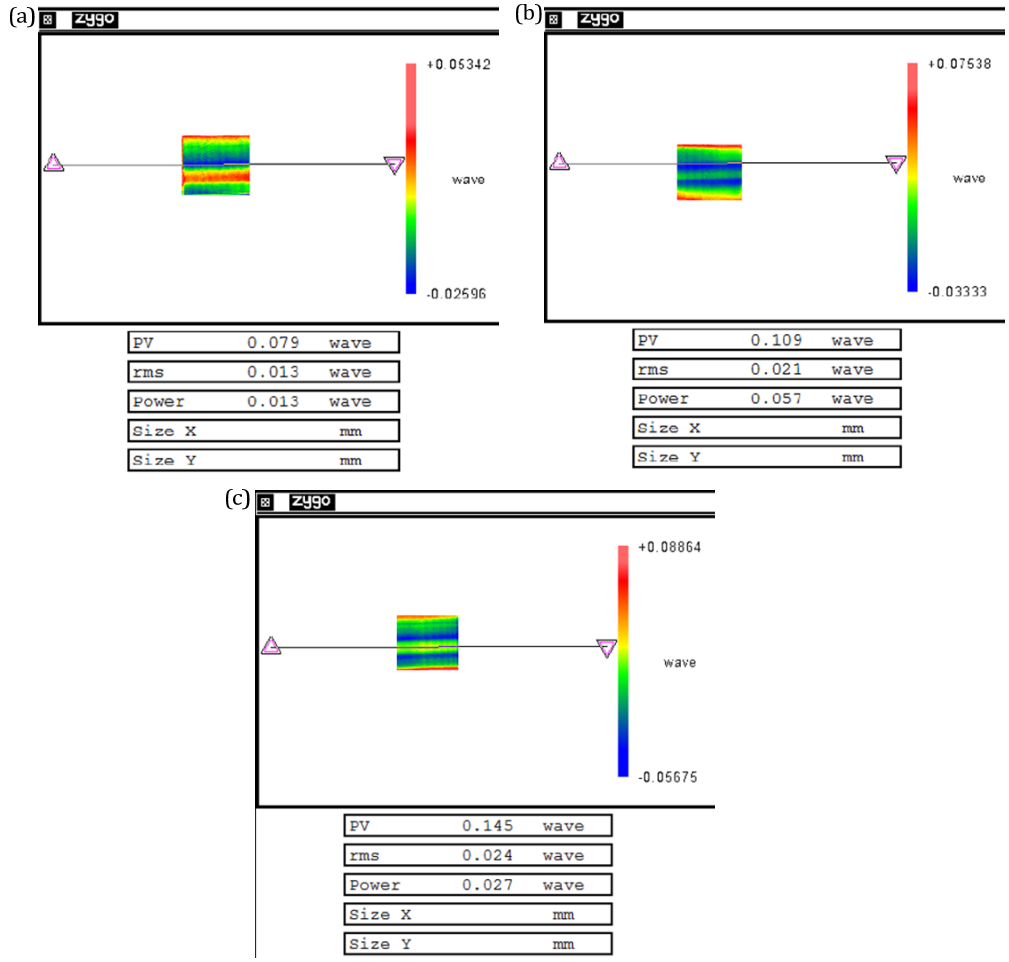

Fig. 9. Wavefront quality of the grating. (a) 500 grooves/mm; (b) 768 grooves/mm; and (c) 1520 grooves/mm.

4.2 High-efficiency echelle gratings with high-precision shapes

We fabricated a high-efficiency echelle grating with 64.285 grooves/mm for use with an interferometer designed by Xi'an Institute of Optics and Precision Mechanics of the Chinese Academy of Sciences. The grating blank has dimensions of 32 mm × 80 mm and the grating area at the center of the grating blank is 20 mm × 68 mm. To produce the echelle grating, we used a grating fabrication process that included grating ruling, grating replication and grating cutting steps. We will write another article to discuss the grating fabrication process.

The echelle grating is blazed for 557.7 nm at the eighth order and for 630 nm at the seventh order, and the calculated blaze angle is 8.2°. To evaluate the grating shape quality, the grooves were measured using an atomic force microscope (AFM), with results as shown in Fig. 10. For comparison, we have listed the measured and theoretical values for the grating shape parameters and the diffraction efficiency in Table 1. As shown in Fig. 10 and Table 1, the grating shape is nearly perfect and is close to the theoretically designed shape. The maximum intensity of the ghosts and scattered light can reach 10^{-5}. Figure 11 shows the wavefront value of the gratings at 632.8 nm, a blazed order of −7. As shown in Fig. 11, the peak to valley (PV) value and the root mean square (RMS) value of the grating are 0.093λ and 0.014λ, respectively.

Optics EXPRESS

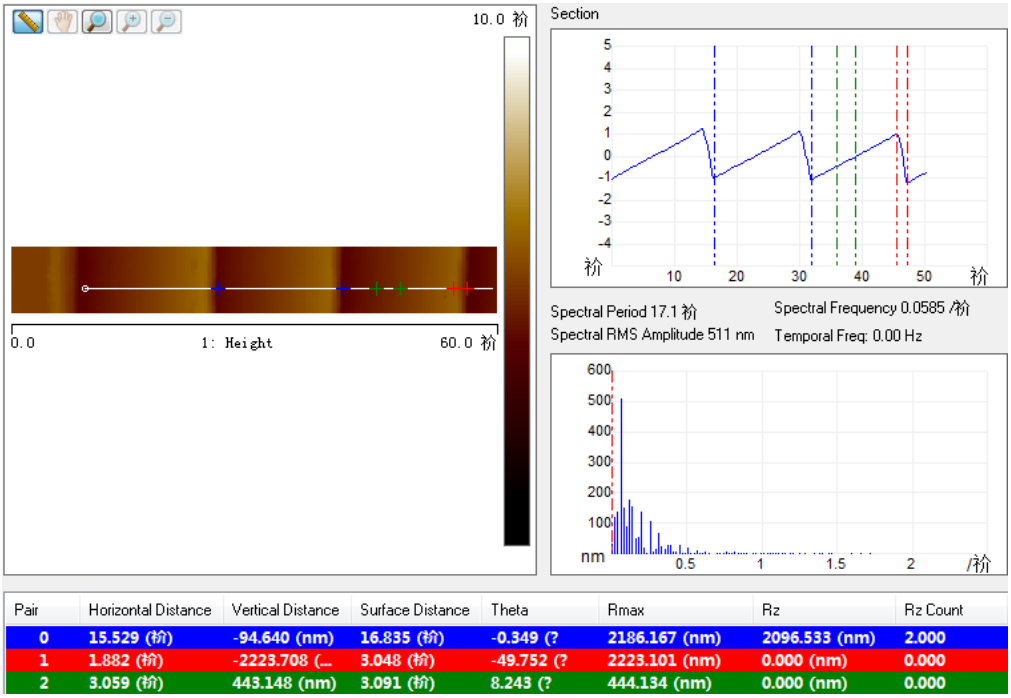

Pair	Horizontal Distance	Vertical Distance	Surface Distance	Theta	Rmax	Rz	Rz Count
0	15.529 (衍)	-94.640 (nm)	16.835 (衍)	-0.349 (?	2186.167 (nm)	2096.533 (nm)	2.000
1	1.882 (衍)	-2223.708 (...	3.048 (衍)	-49.752 (?	2223.101 (nm)	0.000 (nm)	0.000
2	3.059 (衍)	443.148 (nm)	3.091 (衍)	8.243 (?	444.134 (nm)	0.000 (nm)	0.000

Fig. 10. Atomic force microscope test results for a grating with 64.285 grooves/mm.

Table 1. Design values and test values of 64.285 grooves/mm grating.

Parameter	Design Value	Test Value
Grating period	15.5557nm	15.529nm
Groove depth	2196.0135	2223.708nm
Blaze angle	8.2°	8.243°
Efficiency @557.7nm	87.1%	76.82%
Efficiency @630nm	87.59%	75.73%

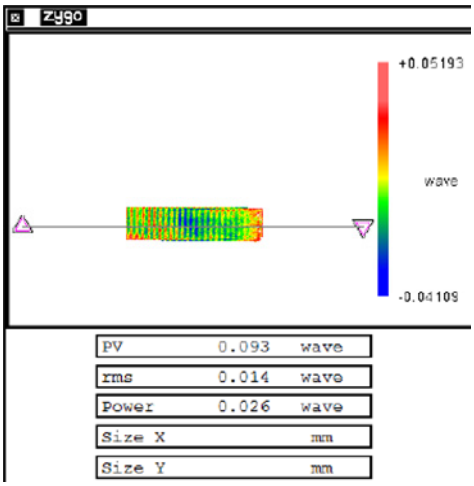

Fig. 11. Wavefront quality of the 64.285-grooves/mm grating.

4.3 Large-area echelle gratings

Recently, we have been developing a 300 mm × 500 mm large-area echelle grating for the spectrometer mounted on the Fiber Arrayed Solar Optical Telescope (FASOT) designed by the

Optics EXPRESS

Yunnan Observatory of the Chinese Academy of Sciences. As the grating area increases, the difficulty of the grating coating and grating ruling processes increases, the grating ruling time becomes longer, and the success rate of grating fabrication will become lower. Any unintended situation at any time could cause the failure of the grating ruling process. For example, a small hard spot on the grating film layer could cause chipping of the blade of the diamond, which would result in the failure of the grating ruling process.

The 300 mm × 500 mm large-area echelle grating has a groove density of 79 grooves/mm and was blazed at 62.6°. After the above improvements are made, the maximum intensity of ghosts and scattered light of the 79-grooves/mm echelle grating reduced to half of that before the improvement. The ghosts are weaker than 10^{-5}, the scattered light intensity can reach 10^{-4}, and the actual efficiency of the echelle grating can reach 90% of the theoretical value. A photograph of the grating is shown in Fig. 12.

Fig. 12. Photograph of the 300 mm × 500 mm grating.

As the grating area increases, the grating wavefront quality will become increasingly important. Zygo interferometer measurement results of the grating at 632.8 nm, a blazed order of −1, are shown in Fig. 13. Figure 13(a) shows the fringes when they are perpendicular to the grooves, and Fig. 13(b) shows the fringes when they are parallel to the grooves. The straightness of the fringes in Figs. 13(a) and 13(b) indicates the accuracy of the grating groove positions and the straightness of the grating grooves. Figures 13(c) and 13(d) show that the peak to valley (PV) value and the root mean square (RMS) value of the grating are 0.289λ and 0.051λ, respectively, the point spread function (PSF) shows that the diffracted energy is concentrated at the center spot, and the Strehl ratio is 0.901.

Optics EXPRESS

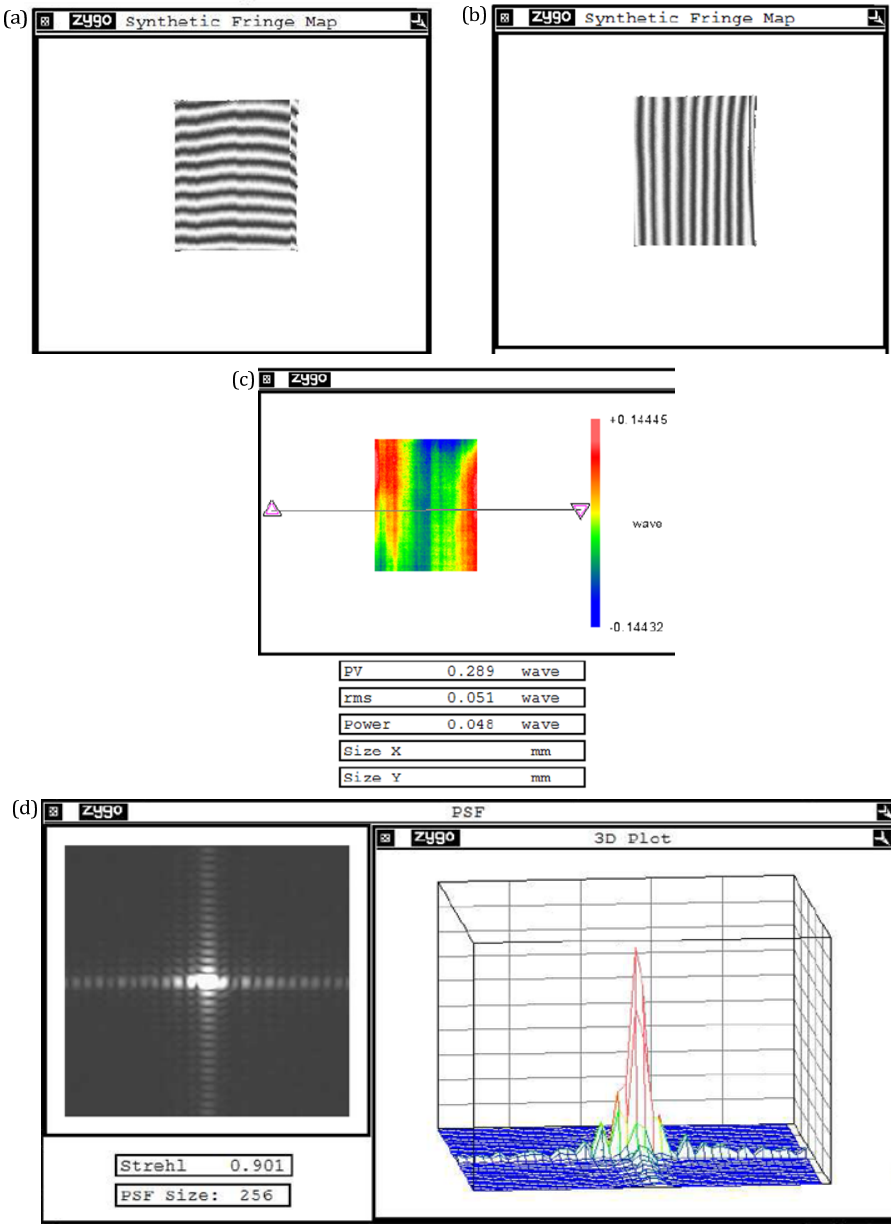

Fig. 13. Wavefront quality of the grating. (a) fringes oriented perpendicular to the grooves; (2) fringes oriented parallel to the grooves;(c) PV and RMS values of the grating; and (d) point spread function (PSF) of the grating.

4.4 High-groove-density gratings

The ruled grating with the highest ruled groove density can directly indicate the accuracy of the ruling engine. After implementation of the improvements described above, the highest achievable groove density when using the grating ruling engine is increased from 6000 grooves/mm to 8000 grooves/mm. The 6000-grooves/mm grating is a 45 mm × 15 mm grating, blazed at 25°. The 8000-grooves/mm grating is a 40 mm × 5 mm grating, blazed at 25°. Because the blazed wavelength of the grating is in the ultraviolet region, the light is easily absorbed by the air, and the diffraction efficiency, the stray light, and the wavefront quality of

Optics EXPRESS

the grating are all difficult to measure. To evaluate the grating quality, the 6000- and 8000-grooves/mm gratings observed via an AFM. As shown in Fig. 14, the positional repeatability of the grooves is excellent, the position errors for 10 grooves of the 6000-grooves/mm grating and the 8000-grooves/mm grating are 4.33 nm and 5 nm, respectively.

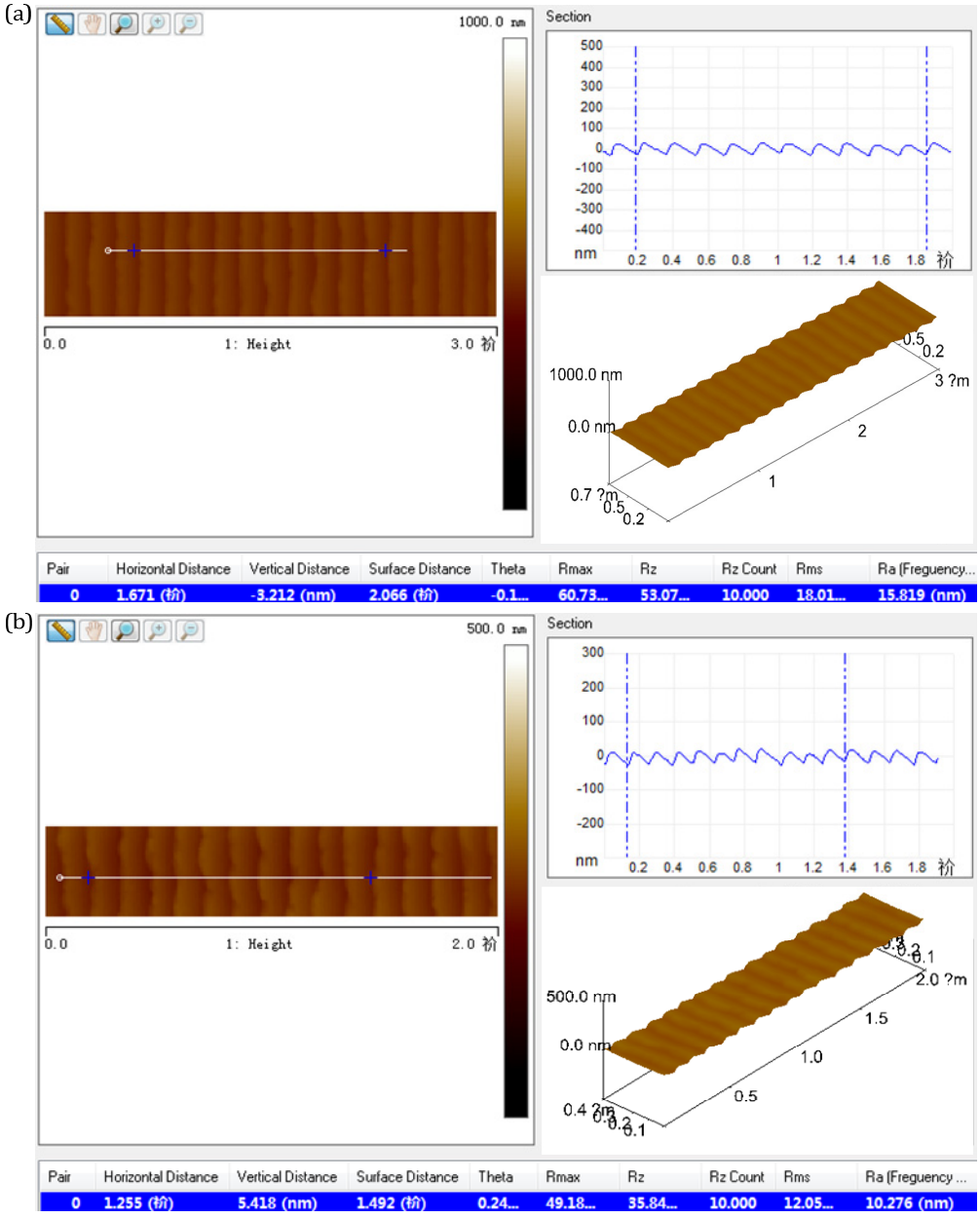

Fig. 14. AFM test results for grating grooves. (a) 6000 grooves/mm. (b) 8000 grooves/mm.

5. Conclusions

To provide further improvement of the accuracy of the CIOMP-6 ruling engine, we have proposed a new concept with the aim of achieving nanometer-level positioning of the grating grooves by controlling the diamond. To implement this new concept, we have designed new

Optics EXPRESS

tool holders, optical path structures, and control methods. The improvement enabled the fabrication of several high-quality gratings, including high-efficiency gratings with groove densities of 500, 768 and 1520 grooves/mm, a 64.285 grooves/mm echelle grating with a high-precision shape and high-efficiency, a 300 mm × 500 mm large-area echelle grating with groove density of 79 grooves/mm, and 6000- and 8000-grooves/mm gratings with high groove densities. After implementation of the improvements, the maximum intensity of ghosts and scattered light of the echelle grating with the density of 79 grooves/mm is reduced to half of that before the improvement, and the highest achievable groove density is increased from 6000 grooves/mm to 8000 grooves/mm. In conclusion, the proposed new concept and the improvements made to the ruling engine have significantly improved the accuracy of the grating ruling engine and the quality of the fabricated gratings.

Funding

Chinese Ministry of National Science and Technology Program (2016YFF0102006, 2016YFF0103304); National Natural Science Foundation of China (NSFC) (61605204, 61505204), The Youth Innovation Promotion Association of CAS (Grant No. 2015174).

Acknowledgments

The authors would like to thank Prof. Zhongquan Qu, Prof. Yutao Feng, and Dr. Yaowu Kuang for their trust and for selecting us to fabricate the gratings that they required. We thank David MacDonald, MSc, from Liwen Bianji, Edanz Editing China (www.liwenbianji.cn/ac), for editing the English text of a draft of this manuscript.

References

1. T. Sakanoi, Y. Kasaba, M. Kagitani, H. Nakagawa, J. Kuhn, and S. Okana, "Development of infrared Echelle spectrograph and mid-infrared heterodyne spectrometer on a small telescope at Haleakala, Hawaii for planetary observation," Proc. SPIE **9147**, 91478D (2014).
2. J. Qiu, X. Qi, X. Li, Z. Ma, Y. Jirigalantu, Y. Tang, X. Mi, X. Zheng, R. Zhang, and Bayanheshig, "Development of a spatial heterodyne Raman spectrometer with echelle-mirror structure," Opt. Express **26**(9), 11994–12006 (2018).
3. B. Zhang, Z. Wang, S. Brodbeck, C. Schneider, M. Kamp, S. Höfling, and H. Geng, "Zero-dimensional polariton laser in a subwavelengh grating-based vertical microcavity," Light Sci. Appl. **3**(1), e135 (2014).
4. F. M. Cheng, J. C. Zhang, D. B. Wang, Z. H. Gu, N. Zhuo, S. Q. Zhai, L. J. Wang, J. Q. Liu, S. M. Liu, F. Q. Liu, and Z. G. Wang, "Demonstration of High-Power and Stable Single-Mode in a Quantum Cascade Laser Using Buried Sampled Grating," Nanoscale Res. Lett. **14**(1), 123 (2019).
5. K. Yang, T. Liu, Z. Wang, G. Li, Y. Han, H. Zhang, and J. Yu, "Five-wavelength –swithable all-fiber erbium-doped laser based on few-mode titled fiber Bragg grating," Opt. Laser Technol. **108**, 273–278 (2018).
6. T. Lei, M. Zhang, Y. Li, P. Jia, G. Ning Liu, X. Xu, Z. Li, C. Min, J. Lin, C. Yu, H. Niu, and X. Yuan, "Massive individual orbital angular momentum channels for multiplexing enabled by Dammann gratings," Light Sci. Appl. **4**(3), e257 (2015).
7. M. Rahlves, A. Günther, M. Rezem, and B. Roth, "Polymer-Based Trasmission Path for Communication and Sensing Applications," J. Lightwave Technol. **37**(3), 729–735 (2019).
8. H. Xu and Y. Shi, "Subwavelength-grating-assisted silicon polarization rotator covering all optical communication bands," Opt. Express **27**(4), 5588–5597 (2019).
9. A. Cotel, M. Castaing, P. Pichon, and C. Le Blanc, "Phased-array grating compression for high-energy chirped pulse amplification lasers," Opt. Express **15**(5), 2742–2752 (2007).
10. J. Qiao, A. W. Schmid, L. J. Waxer, T. Nguyen, J. Bunkenburg, C. Kingsley, A. Kozlov, and D. Weiner, "In situ detection and analysis of laser-induced damage on a 1.5-m multilayer-dielectric grating compressor for high-energy, petawatt-class laser systems," Opt. Express **18**(10), 10423–10431 (2010).
11. D. Nevejans, E. Neefs, E. Van Ransbeeck, S. Berkenbosch, R. Clairquin, L. De Vos, W. Moelans, S. Glorieux, A. Baeke, O. Korablev, I. Vinogradov, Y. Kalinnikov, B. Bach, J.-P. Dubois, and E. Villard, "Compact high-resolution spaceborne echelle grating spectrometer with acousto-optical tunable filter based order sorting for the infrared domain from 2.2 to 4.3 microm," Appl. Opt. **45**(21), 5191–5206 (2006).
12. S. Zhang, X. Mi, Q. Zhang, S. Jirigalantu, S. Feng, H. Yu, and X. Qi, "Groove shape characteristics of echelle gratings with high diffraction efficiency," Opt. Commun. **387**, 401–404 (2017).
13. T. Jitsuno, S. Motokoshi, T. Okamoto, T. Mikami, D. Smith, M. L. Schattenburg, H. Kitamura, H. Matsuo, T. Kawasaki, K. Kondo, H. Shirage, Y. Nakata, H. Habara, K. Tsubakimoto, R. Kodama, K. A. Tanaka, N. Miyanga, and K. Mima, "Development of 91 cm size gratings and mirrors for LEFX laser system," J. Phys. Conf. Ser. **112**(3), 032002 (2008).

Optics EXPRESS

14. C. H. Chang, Y. Zhao, R. K. Heilmann, and M. L. Schattenburg, "Fabrication of 50 nm period gratings with multilevel interference lithography," Opt. Lett. **33**(14), 1572–1574 (2008).
15. C. R. Englert, C. M. Brown, B. Bach, E. Bach, K. Bach, J. M. Harlander, J. F. Seely, K. D. Marr, and I. Miller, "High-efficiency echelle gratings for MIGHTI, the spatial heterodyne interferometers for the ICON mission," Appl. Opt. **56**(8), 2090–2098 (2017).
16. S. V. Bykov, B. Sharma, and S. A. Asher, "High-Throughput, High-Resolution Echelle deep-UV Raman Spectrometer," Appl. Spectrosc. **67**(8), 873–883 (2013).
17. M. V. Zorina, S. Y. Zuev, M. S. Mikhailenko, A. E. Pestov, V. N. Polkovnikov, N. N. Salashchenko, and N. I. Chkhalo, "The diffraction efficiency of echelle gratings increased by ion-beam polishing of groove surfaces," Tech. Phys. Lett. **42**(8), 844–847 (2016).
18. C. Yang, X. Li, H. Yu, H. Yu, J. Zhu, S. Zhang, J. Gao Bayanheshig, and Y. Tang, "Practical method study on correcting yaw error of 500 mm grating blank carriage in real time," Appl. Opt. **54**(13), 4084–4088 (2015).
19. X. Mi, H. Yu, H. Yu, S. Zhang, X. Li, X. Yao, X. Qi, Bayinhedhig, and Q. Wan, "Correcting groove error in gratings ruled on a 500-mm ruling engine using interferometric control," Appl. Opt. **56**(21), 5857–5864 (2017).
20. G. R. Harrison, "The Production of Diffraction Gratings I. Development of the Ruling Art," J. Opt. Soc. Am. **39**(6), 413–426 (1949).
21. C. Mitchell, "Diffraction grating fabrication in Australia," Spectrochim. Acta B At. Spectrosc. **54**(14), 2041–2049 (1999).
22. X. Li, H. Yu, X. Qi, S. Feng, J. Chui, S. Z. Jirigalantu, and Y. Tang, "300 mm ruling engine producing gratings and echelles under interferometric control in China," Appl. Opt. **54**(7), 1819–1826 (2015).
23. X. Mi, S. Zhang, H. Yu, H. Yu, M. Cong, and X. Qi, "Using a unique mirror to minimize the effect of ruling engine cosine error on grating performance," Appl. Opt. **57**(35), 10146–10151 (2018).
24. D. A. Davies and G. M. Stiff, "Diffraction Grating Ruling in Australia," Appl. Opt. **8**(7), 1379–1384 (1969).
25. W. R. Horsfield, "Ruling Engine with Hydraulic Drive," Appl. Opt. **4**(2), 189–193 (1965).
26. H. W. Babcock, "Control of a ruling engine by a modulated interferometer," Appl. Opt. **1**(4), 415–420 (1962).
27. G. R. Harrison and S. W. Thompson, "Large diffraction gratings ruled on a commercial measuring machine controlled interferometrically," J. Opt. Soc. Am. **60**(5), 591–595 (1970).
28. G. R. Harrison, S. W. Thompson, H. Kazukonis, and J. R. Connell, "750-mm ruling engine producing large gratings and echelles," J. Opt. Soc. Am. **62**(6), 751–756 (1972).
29. T. Kita and T. Harada, "Ruling engine using a piezoelectric device for large and high-groove density gratings," Appl. Opt. **31**(10), 1399–1406 (1992).